

# Noninvasive Estimation of Aortic Pressure Waveform Based on Simplified Kalman Filter and Dual Peripheral Artery Pressure Waveforms

Wenyan Liu<sup>a</sup>, Shuo Du<sup>a</sup>, Shuran Zhou<sup>a</sup>, Tiemin Mei<sup>d,\*</sup>, Yuelan Zhang<sup>e</sup>, Guozhe Sun<sup>e</sup>, Shuang Song<sup>f</sup>, Lisheng Xu<sup>a,b,c,\*</sup>, Stephen E. Greenwald<sup>g</sup>, Yudong Yao<sup>a</sup>

<sup>a</sup> College of Medicine and Biological and Information Engineering, Northeastern University, Shenyang 110169, China

<sup>b</sup> Key Laboratory of Medical Image Computing, Ministry of Education, Shenyang 110169, China

<sup>c</sup> Neusoft Research of Intelligent Healthcare Technology, Co. Ltd., Shenyang 110169, China

<sup>d</sup> School of Automation and Electrical Engineering, Shenyang Ligong University, Shenyang 110159, China

<sup>e</sup> First Hospital of China Medical University, Shenyang 110122, China

<sup>f</sup> School of Mechanical Engineering and Automation, Harbin Institute of Technology Shenzhen Graduate School, Shenzhen 518055, China

<sup>g</sup> Blizzard Institute, Barts & The London School of Medicine & Dentistry, Queen Mary University of London, United Kingdom

---

## ARTICLE INFO

### Keywords:

Aortic pressure  
Peripheral artery pressure  
Simplified Kalman filter  
Canonical correlation analysis  
Signal-to-noise ratio  
Noise-tolerance

## A B S T R A C T

*Background and Objective:* Aortic pressure ( $P_a$ ) is important for the diagnosis of cardiovascular disease. However, its direct measurement is invasive, not risk-free, and relatively costly. In this paper, a new simplified Kalman filter (SKF) algorithm is employed for the reconstruction of the  $P_a$  waveform using dual peripheral artery pressure waveforms.

*Methods:*  $P_a$  waveforms obtained in a previous study were collected from 25 patients. Simultaneously, radial and femoral pressure waveforms were generated from two simulation experiments, using transfer functions. In the first, the transfer function is a known finite impulse response; and in the second, it is derived from a tube-load model. To analyse the performance of the proposed SKF algorithm, variable amounts of noise were added to the observed output signal, to give a range of signal-to-noise ratios (SNRs). Additionally, central aortic, brachial and femoral pressure waveforms were simultaneously collected from 2 Sprague-Dawley rats and the measured and reconstructed  $P_a$  waveforms were compared.

*Results:* The proposed SKF algorithm outperforms canonical correlation analysis (CCA), which is the current state-of-the-art blind system identification method for the non-invasive estimation of central aortic blood pressure. It is also shown that the proposed SKF algorithm is more noise-tolerant than the CCA algorithm over a wide range of SNRs.

*Conclusion:* The simulations and animal experiments illustrate that the proposed SKF algorithm is accurate and stable in the face of low SNRs. Improved methods for estimating central blood pressure as a measure of cardiac load adds to their value as a prognostic and diagnostic tool.

---

## 1. Introduction

The aortic pressure ( $P_a$ ) waveform is an important predictor of cardiovascular disease risk [1]. The blood ejected from the left ventricle gives rise to an aortic pressure wave which is propagated through the arterial tree changing in amplitude and shape as it progresses, in a way which depends on variations in the local diameter, wall thickness and elastic properties of the aorta, as well as the presence of reflected waves from peripheral sites and, to a lesser extent, on re-reflections [2], [3]. Thus  $P_a$ , having been formed initially at the aortic root by the contraction of the left ventricle, contains essential information about the heart itself as well as about the properties of the arterial system in general [4], [5].  $P_a$  in the ascending aorta, often referred to as “central pressure” is of particular importance because it is a measure of maximal left ventricular load [6]. However, the use of  $P_a$  as a diagnostic and prognostic tool has been limited in clinical practice because the gold standard of  $P_a$  measurement using a pressure-sensing cardiac catheter is invasive and expensive [7]. Therefore, a number of non-invasive measurement techniques have been proposed, usually substitution and transfer function methods in which the central pressure wave is derived from peripheral pressure measurements. Peripheral artery pressure ( $P_p$ ) waveforms such as the brachial ( $P_b$ ) are generally easier to obtain noninvasively than the  $P_a$  waveform. However, due to the aforementioned changes in shape as the wave propagates along the arterial tree, important aspects of the  $P_a$  waveform, such as systolic pressure and pulse pressure cannot be accurately derived from the measurement of peripheral artery pressure [8]. Carotid pressure is also

often used as a surrogate for central  $P_a$  because the carotid artery is closer to the aorta than the brachial. However, even the carotid pressure waveform is subject to amplification and, in general, will lead to an over-estimation of central  $P_a$  [9], [10]. Several numerical methods to estimate the  $P_a$  from non-invasive measurements of  $P_p$  have recently been developed. A widely used approach is based on the notion of a generalized transfer function. This is obtained from simultaneous measurements of  $P_a$  (invasive) and  $P_p$  (non-invasive) on a large number of subjects [11], [12], [15]. The inverse transfer function can then be derived and used to estimate  $P_a$  from  $P_p$ . Tube-load models represent the path between the aorta and the periphery from which a transfer function can be derived for the  $P_a$  waveform [13], [14]. However, generalized transfer function methods require parameter values derived from prior invasively measured central pressures from many subjects [15]. Additionally, the form of the function will depend on the specific measurement device and thus care should be taken to allow for this [15]. Furthermore, it is usually assumed that the arterial system is linear and short-time invariant. In spite of these limitations, such methods have proved to be useful as a means of estimating systolic pressure although pulse pressure estimation is less reliable [17]. More recently, multichannel blind system identification (MBSI) algorithms have been proposed, such as the cross-relation (CR) algorithm [18], the subspace (SS) algorithm [19], and the canonical correlation analysis (CCA) algorithm [20]. These methods are able to estimate the  $P_a$  waveform satisfactorily when the signal-to-noise ratio (SNR) of the observed channel output is high [21]. Unfortunately, the peripheral artery pressure signal may contain some noise and the SNR

may not be high enough. In this paper, we propose a simplified Kalman filter (SKF) algorithm for  $P_a$  waveform estimation with a high update rate and which is tolerant of low SNRs.

The paper is organized as follows. Section 2 describes the data acquisition, the estimation of the  $P_a$  by the MBSI method, evaluation indices and statistical analysis. Section 3 presents the results, which are discussed and interpreted in Section 4. Section 5 concludes the paper with suggestions for future work.

## 2. Methods

In this paper, the CCA algorithm [20] based on a linear single input multiple output (SIMO) system is applied as a benchmark to compare the performance of different blind system identification algorithms. The generated peripheral artery pressure waveforms as the observed output signals using the finite impulse response (FIR) and tube-load simulation models are noiseless. It has been reported that the majority of real pulse waveforms have SNRs between 50 dB and 10 dB with only 8% above 50 dB and only 1.5% below 10 dB [22]. Therefore, to analyze and compare the performance of the SKF and CCA algorithms, various levels of noise (Gaussian random) in the range 10 dB to 50 dB were added to the observed output signals. Respiration was simulated by modulating the baseline with a sinusoidal signal [22]. and these noisy signals were used in the simulation experiments. With this in mind, the resulting pulse signal can be modeled as:

$$x_i(n) = p_{pi}(n) + b_{1i}(n) + b_{2i}(n) \quad (1)$$

As shown in Fig. 1,  $p_{pi}(n)$  represents the heart-generated pulse wave signal.  $b_{1i}(n)$  and  $b_{2i}(n)$  represent the respiratory modulation signal and Gaussian random noise signal, respectively.

$$b_{1i}(n) = a_1 \sin(2\pi f_0 n / F_s) \quad (2)$$

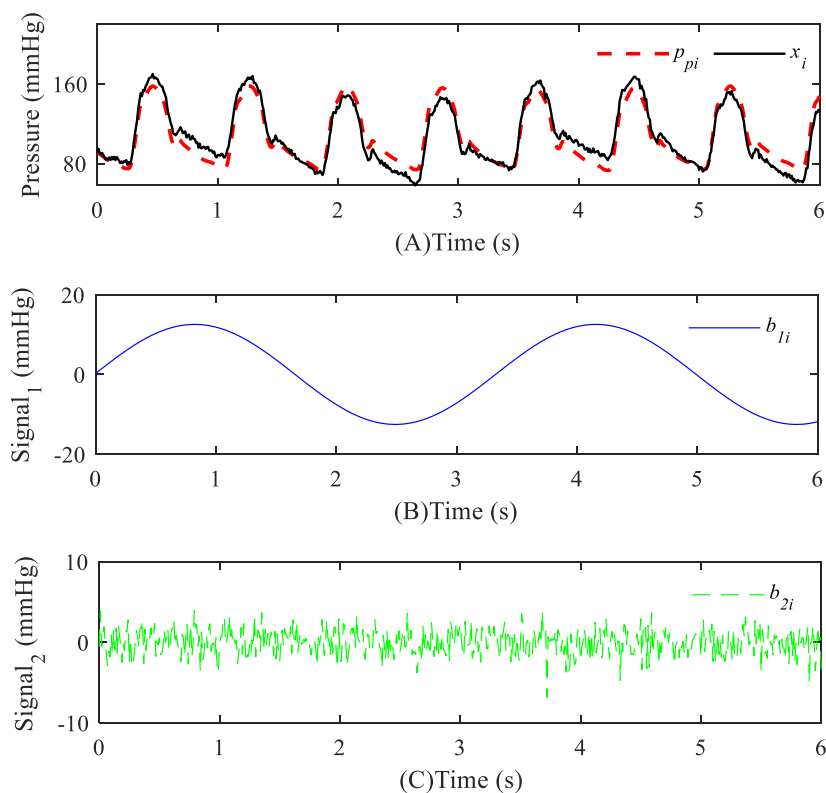


**Fig. 1.** Examples of a pulse wave, simulated baseline modulation and Gaussian random noise signals (SNR =25 dB).  $p_{pi}$ : pulse wave signal without noise;  $x_i$ : pulse wave signal with added Gaussian noise and respiratory modulation.  $b_{1i}$ : simulated respiratory modulation signal;  $b_{2i}$ : Gaussian random noise signal.

where  $a_1$  and  $f_0$  are the amplitude and frequency of the simulated respiratory sinusoidal signal. Clinical observations have shown that the

healthy human pulse rate is four to five times the respiration rate [23]. Therefore,  $f_0$  was set to 0.3 Hz and the value of  $a_1$  was chosen according to the magnitude of the SNR.

### 2.1 Data acquisition

Here, we have utilized a set of clinical data collected in a previous study [24], [40]. Invasive measurements of central  $P_a$  were made at the aortic root in 25 patients undergoing cardiac surgery, at a sampling frequency of 100 Hz. Basic population and hemodynamic data are listed in Table 1. Approval was obtained from the Research Ethics Committee of the Northeastern University (EC-2020B016), China, and written informed consent was obtained from all participants.

**Table 1**

Basic information of the clinical data (Mean  $\pm$  SD).

| Variables       | Data             |
|-----------------|------------------|
| No. of subjects | 25               |
| Age (years)     | 56.8 $\pm$ 13.5  |
| Height (cm)     | 165.4 $\pm$ 7.9  |
| Weight (kg)     | 68.6 $\pm$ 12.4  |
| SP (mmHg)       | 147.3 $\pm$ 20.7 |
| DP (mmHg)       | 76.8 $\pm$ 11.5  |
| HR (bpm)        | 74.0 $\pm$ 4.8   |

#### 2.1.1 Simulation data generated with the FIR model

As shown in Fig. 2, the simulated radial pressure ( $P_r$ ) and femoral pressure ( $P_f$ ) waveforms without noise are obtained as the output signals of two given FIRs with the above-mentioned  $P_a$  waveform as the input signal. The impulse responses of the two channels, were as used in a previous study [20]. The FIR coefficients refer to the pressure signal transmission from the aorta to the upper and lower limb arteries, respectively.

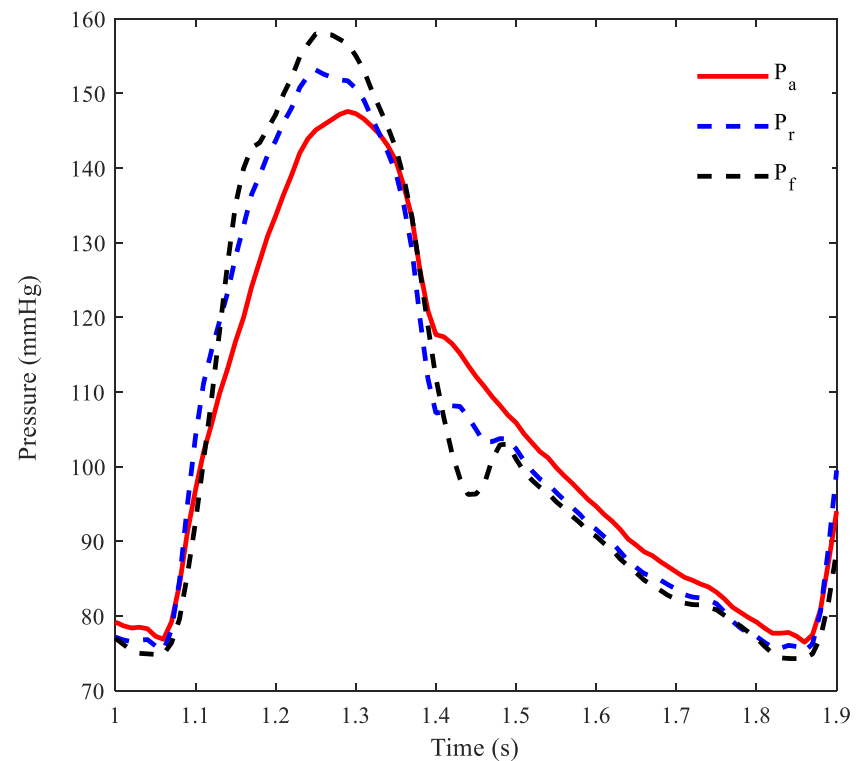


**Fig. 2.** Measured  $P_a$  and generated  $P_r$  and  $P_f$  waveforms using the FIR simulation model.

#### 2.1.2 Simulation data generated with the tube-load model

The ascending aortic to peripheral wave propagation path is modeled by a uniform lossless tube and a Windkessel load. This set up is usually called the tube-load model, the transfer function of which is given by:

$$G(z) = \frac{P_p(z)}{P_a(z)} = \frac{z^{N_{a-p}+1} + [(\eta_1 + \eta_2)/F_s - 1]z^{N_{a-p}}}{z^{2N_{a-p}+1} + (\eta_1/F_s - 1)z^{2N_{a-p}} + \eta_2/F_s} \quad (3)$$

Derivation of the equations and further details can be found in [14]. The transfer function of the tube-load model has three unknown parameters:  $N_{a-p}$ ,  $\eta_1$  and  $\eta_2$ . In Equation (4),  $Z_c$  represents the characteristic impedance of the tube, the terminal of which is composed of a Windkessel load consisting of the compliance ( $C_T$ ) of the distal arteries and a peripheral resistance ( $R_T$ ) due to the arterioles.  $Z_L$  represents the terminal impedance of the Windkessel load. In Equation (5),  $n_{a-p}$  is the pulse transit time associated with the wave propagation from the ascending aorta to the distal end of the cardiovascular system.  $F_s$  is the sampling frequency.

$$\eta_1 = \frac{2Z_c + R_T}{2Z_c \cdot R_T \cdot C_T}, \quad \eta_2 = \frac{R_T}{2Z_c \cdot R_T \cdot C_T} \quad (4)$$

$$N_{a-p} = n_{a-p} \cdot F_s, \quad N_L = 2N_{a-p} + 1 \quad (5)$$

In many previous studies, the tube-load model has been used in animals to estimate central aortic hemodynamics based on the relative ease of obtaining  $P_p$  waveforms [25], [33]-[35]. The model has been rarely used in human subjects due to the difficulty of obtaining invasive aortic pressure measurements and simultaneous multiple peripheral artery pressures. In one such study [14], the values of the physiologically relevant parameters of the tube-load model (load compliance, characteristic impedance, and peripheral resistance, pulse transit time etc.) were derived from the measured aortic blood pressure and estimated aortic blood pressure. The mean values of the parameters such as  $\eta_1$ ,  $\eta_2$  and  $n_{a-p}$  from this study [14] are used in this simulation. Their values are 94.6 and 16.6 for radial artery; and 82.5 and 40.6 for the femoral artery. The order  $N_L$  of the transfer function is determined by the values of the parameter  $n_{a-p}$  for the upper and lower limbs. The  $n_{a-p}$  of the upper and lower limbs were set to 86.9 ms and 64.4 ms, respectively. The same  $P_a$  waveform in subsection 2.1.1 was also used as the input signal to the tube-load models. The simulated waveforms are shown in Fig. 3.

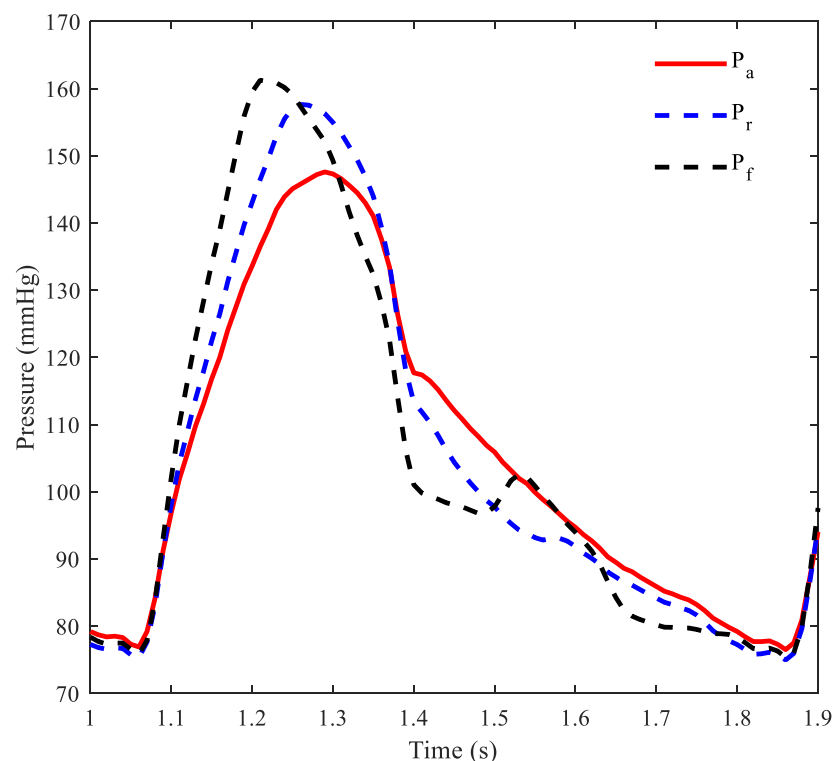


Fig. 3. An example of measured  $P_a$  waveform and the corresponding simulated  $P_r$  and  $P_f$  waveforms based on the tube-load model.

### 2.1.3 Animal experiments

Blood pressure in the ascending aorta, brachial and femoral arteries was recorded in two anesthetized Sprague-Dawley rats, weighing 0.32 kg and 0.35 kg. Blood pressures were measured simultaneously through three catheters, each connected to a transducer (MLT1199, AD Instruments, Castle Hill Australia). The catheters were introduced via incisions in the right common carotid artery and right brachial and left femoral arteries. The carotid catheter (outer diameter (o.d.) 0.90 mm and an inner diameter (i.d.) 0.50 mm.) was passed into the ascending aorta to record aortic pressure. For the brachial and femoral artery measurements, smaller catheters, o.d. 0.60 mm and i.d. 0.30 mm were used. A Power Lab 8/35 (PL3508) and quad Bio Amp (FE224) acquisition system (AD Instruments, Castle Hill Australia) and Lab Chart software running on a laptop computer were used for displaying and storing the data in real time, at a sampling rate of 1 kHz. All the animal experimental procedures were approved by the Institutional Animal Care and Use Committee (IACUC) of Shenzhen Institutes of Advanced Technology, Chinese Academy of Sciences: (SIAT-IACUC-190801-YGS-LWH-A0454-01).

### 2.2 Estimation of the $P_a$ by the MBSI algorithm

In this study, the cardiovascular system is regarded as a black-box model of a two-channel wave propagation system, with one channel corresponding to the upper limb and the other to the lower limb. Up to now, many MBSI approaches have assumed the arterial system to be linear and short-time invariant [20]. In this study, we present a method for  $P_a$  waveform estimation, with a FIR filter used as a transfer function. For a two-channel FIR system as presented in Fig. 4,  $s(n)$  denotes the  $P_a$  waveform;  $x_i(n)$ , ( $i=1, 2$ ) denotes the  $P_p$  waveforms; the  $L$ -by-1 vector  $\mathbf{h}_i = [h_i(0), h_i(1), \dots, h_i(L-1)]^T$ , ( $i=1, 2$ ) represents the channel's impulse response between the  $P_a$  waveform and the  $i$ -th  $P_p$  waveform;  $u_i(n)$  is the additive noise.

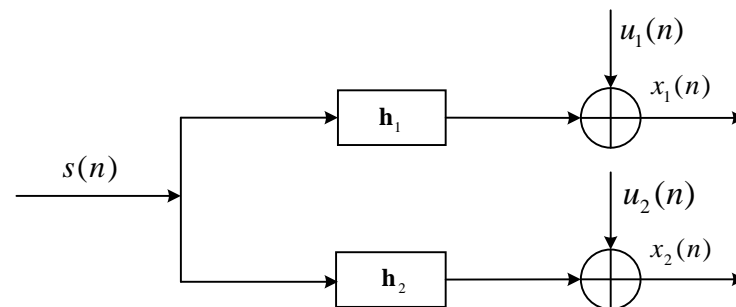


Fig. 4. Black-box structure of a two-channel FIR system.

A linear convolution between the  $P_a$  and  $P_p$  waveforms is then given by Equation (6) [26]:

$$x_i(n) = \sum_{k=0}^{L-1} h_i(k)s(n-k) + u_i(n) \quad (6)$$

The two  $P_p$  waveforms are not independent; they conform to the so-called cross-relation (CR):

$$x_1(n) * h_2(n) = x_2(n) * h_1(n) + \theta_{12}(n) \quad (7)$$

where

$$\theta_{12}(n) = u_1(n) * h_2(n) - u_2(n) * h_1(n) \quad (8)$$

The  $*$  symbol is the linear convolution operator. The cross-relation in Equation (7) can be rewritten in matrix form as:

$$\mathbf{C}(n)\mathbf{h} + \theta_{12}(n) = 0 \quad (9)$$

where  $\mathbf{C}(n) = [\mathbf{x}_2(n), -\mathbf{x}_1(n)]$ ;  $\mathbf{h} = [\mathbf{h}_1^T, \mathbf{h}_2^T]^T$ ;  $\mathbf{x}_i(n) = [x_i(n), x_i(n-1), \dots, x_i(n-L+1)]$ .

### 2.2.1 An introduction to the SKF algorithm

For  $P_a$  waveform estimation, the first step is to identify the multichannel impulse response vector  $\mathbf{h}$ . Taking into account the cross-relation in Equation (9), we propose the following Kalman filter problem for  $\mathbf{h}$  estimation. The process and measurement equations are given as follows:

a) Process equation:

$$\mathbf{h}(n+1) = \mathbf{F}(n+1, n)\mathbf{h}(n) + \mathbf{v}_1(n) \quad (10)$$

b) Measurement equation:

$$\mathbf{y}(n) = \mathbf{C}(n)\mathbf{h}(n) + \mathbf{v}_2(n) \quad (11)$$

where the vectors  $\mathbf{v}_1(n)$  and  $\mathbf{v}_2(n) = \theta_{12}(n)$  denote the process and measurement noise, respectively; the state transition matrix is assumed to be  $\mathbf{F}(n+1, n) = \mathbf{I}$  (identity matrix) because the cardiovascular system is a slow time-varying system; the observation vector  $\mathbf{y}(n) = \mathbf{0}$  ( $n = 1, 2, \dots$ ) is a zero-vector series. For the special transition matrix and the zero-observation vector, the computation of the Kalman filter is simplified as in Table 2.

**Table 2**  
Summary of the SKF algorithm.

|                                                                                                                                         |
|-----------------------------------------------------------------------------------------------------------------------------------------|
| Input vector process:                                                                                                                   |
| $x_1(n), x_2(n)$                                                                                                                        |
| Known parameters:                                                                                                                       |
| $\mathbf{F}(n+1, n) = \mathbf{I}$                                                                                                       |
| $\mathbf{Q}_1(n) = 0, \mathbf{Q}_2(n) = \begin{cases} 10^{-7} \mathbf{I}, & \text{Noiseless} \\ \mathbf{I}, & \text{Noisy} \end{cases}$ |
| Computation: $n = 1, 2, 3, \dots$                                                                                                       |
| $\mathbf{G}(n) = \mathbf{K}(n-1)\mathbf{C}^T(n)[\mathbf{C}(n)\mathbf{K}(n-1)\mathbf{C}^T(n) + \mathbf{Q}_2(n)]^{-1}$                    |
| $\hat{\mathbf{h}}(n+1) = \hat{\mathbf{h}}(n) - \mathbf{G}(n)\mathbf{C}(n)\hat{\mathbf{h}}(n)$ , here $\ \hat{\mathbf{h}}\ _2 = 1$       |
| $\mathbf{K}(n) = \mathbf{K}(n-1) - \mathbf{G}(n)\mathbf{C}(n)\mathbf{K}(n-1)$                                                           |

As shown in Table 2, for the simplified multichannel identification problem, the correlation matrix of process noise is assumed to be  $\mathbf{Q}_1(n) = 0$  (meaning  $\mathbf{v}_1(n) = 0$ ) and the correlation matrix of the measurement noise is assumed to be  $\mathbf{Q}_2(n)$ . The matrix  $\mathbf{G}(n)$  represents the Kalman gain, and the  $\mathbf{K}(n)$  represents the filtered state-error correlation matrix.

### 2.2.2 Multichannel deconvolution algorithm

After the identifying the SIMO system using the SKF algorithm, the  $P_a$  waveform can be obtained by the deconvolution of the two known  $P_p$  waveforms. These deconvolution problems are of two types. First, if both the output signal and the channel responses are known, the input signal can be solved by ordinary deconvolution. Second, if only the output signal is known, both the input signal and the channel transfer function need to be solved. This second type is known as blind deconvolution and is more difficult to handle than ordinary deconvolution. Nevertheless, multichannel blind deconvolution algorithms have been used in many applications including signal processing [27], medical imaging [28] and seismic imaging [29]. Several blind deconvolution algorithms have been proposed, including the Sato algorithm [30], Godard algorithm [31] as well as Bussgang-type algorithms [32]. However, these algorithms require prior knowledge of the source statistics. The multi-input multi-output theorem can also be used to solve a multichannel inverse system and then to filter multiple signals [33]. In this paper, the channel responses are solved by the SKF algorithm. Both two-channel output signals and the corresponding two FIRs are known and used to solve the common input

signal based on a multichannel least squares deconvolution. Equation (6) can be rewritten in matrix form:

$$\begin{bmatrix} \mathbf{x}_1 \\ \mathbf{x}_2 \end{bmatrix} = \begin{bmatrix} \mathbf{H}_1 \\ \mathbf{H}_2 \end{bmatrix} \mathbf{s} + \begin{bmatrix} \mathbf{u}_1 \\ \mathbf{u}_2 \end{bmatrix} \quad (12)$$

where

$$\mathbf{x}_i = [x_i(0), x_i(1), \dots, x_i(N-1)]^T \quad (13)$$

$$\mathbf{u}_i = [u_i(0), u_i(1), \dots, u_i(N-1)]^T \quad (14)$$

$$\mathbf{s} = [s(-L+1), s(-L+2), \dots, s(N-1)]^T \quad (15)$$

and  $N$  denotes the number of the measured  $P_p$  waveform samples.

$$\mathbf{H}_i = \begin{bmatrix} h_i(L-1) & \dots & h_i(0) & \dots & \dots & 0 \\ 0 & h_i(L-1) & \dots & h_i(0) & \dots & 0 \\ \dots & \dots & \dots & \dots & \dots & \dots \\ 0 & \dots & \dots & h_i(L-1) & \dots & h_i(0) \end{bmatrix} \quad (16)$$

Here  $\mathbf{H}_i$  is the  $[N \times (N+L-1)]$  Toeplitz matrix composed of the estimated impulse responses of the channel. The linear least squares solution of the problem is given by:

$$\mathbf{s} = (\mathbf{H}^T \mathbf{H})^{-1} \mathbf{H}^T \mathbf{x} \quad (17)$$

where

$$\mathbf{H} = [\mathbf{H}_1^T, \mathbf{H}_2^T]^T \quad (18)$$

$$\mathbf{x} = [\mathbf{x}_1^T, \mathbf{x}_2^T]^T \quad (19)$$

### 2.2.3 Evaluation and statistical analysis

In all experiments, we used the root mean square error (RMSE) as a measure of the quality of the quantitative assessments. RMSE is defined as follows:

$$\text{RMSE} = \sqrt{\frac{1}{N} \sum_{n=1}^N [s(n) - \hat{s}(n)]^2} \quad (20)$$

In Equation (20),  $s(n)$  is the real source input signal for the system identification;  $\hat{s}(n)$  is the estimated source input signal and  $N$  represents the total number of data points comprising the test signal.

Normalized projection misalignment (NPM) is commonly used to evaluate the convergence performance of the estimated impulse responses in blind SIMO systems [36], [37]. The NPM is computed during the iteration process and is given by:

$$\text{NPM}_i(k) = 20 \log_{10} \left\| \frac{\mathbf{h}_i - \frac{\mathbf{h}_i^T \hat{\mathbf{h}}_i(k)}{\hat{\mathbf{h}}_i^T(k) \hat{\mathbf{h}}_i(k)} \hat{\mathbf{h}}_i(k)}{\|\mathbf{h}_i\|} \right\| \quad (21)$$

where  $\|\cdot\|$  is the  $l_2$  norm;  $k$  is the iteration index;  $\mathbf{h}_i$  and  $\hat{\mathbf{h}}_i$  are the real and estimated FIRs, respectively.

Measured and estimated central aortic pressure were analyzed by a paired t-test (IBM SPSS Statistics, version-23) and reported as mean  $\pm$  SD or 95% CI where appropriate. The linear regression analysis and Pearson's correlation coefficients measured and estimated central aortic pressure were also calculated. Bland-Altman plots were constructed to assess the agreement between estimated and measured central aortic pressure. A p-value smaller than 0.001 was considered to be statistically significant.

## 3. Results

### 3.1 FIR simulation experiments

Blind system identification algorithms are usually sensitive and vulnerable to measurement noise [21]. The SNR of the observed output signals can affect the convergence process and the noise of each channel is unknown in practice. Therefore, simulation experiments were conducted to verify the performance of the proposed algorithm under a range of different SNRs. In Fig. 5, the curves represent the convergence performance of the SKF algorithm when applied to signals with various SNRs. The curves from top to bottom correspond to SNRs from 10 dB to 50 dB. Fig. 6 shows the effect of iteration number on the relationship between RMSE and SNR, using the SKF algorithm. As shown in Fig. 6, the number of iterations is in the range 80 to 200.

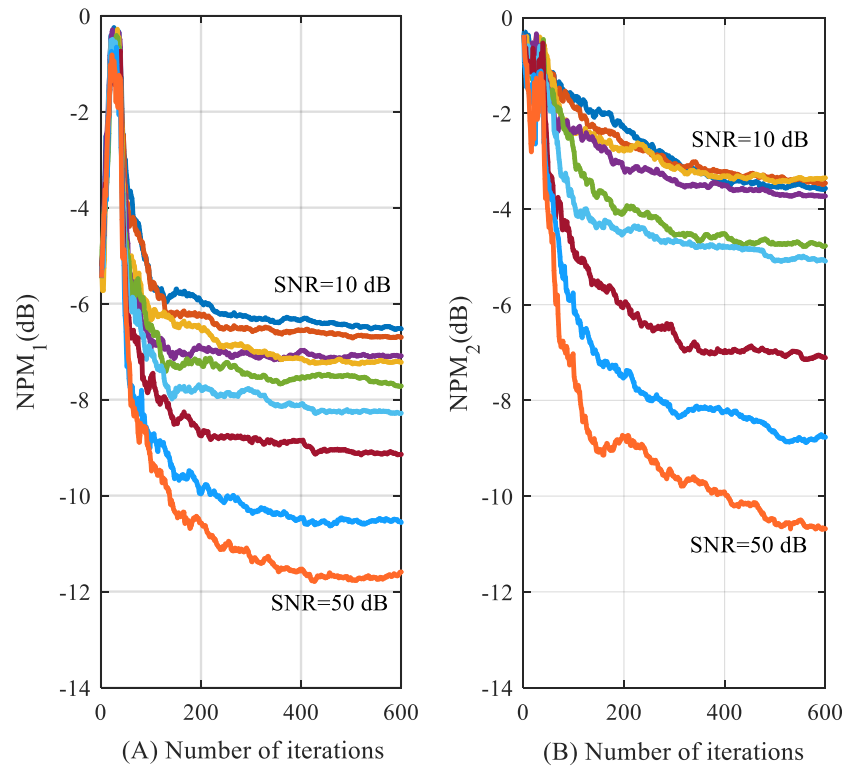


**Fig. 5.** The convergence behavior of averaged NPMs at different SNRs for a two-channel system.

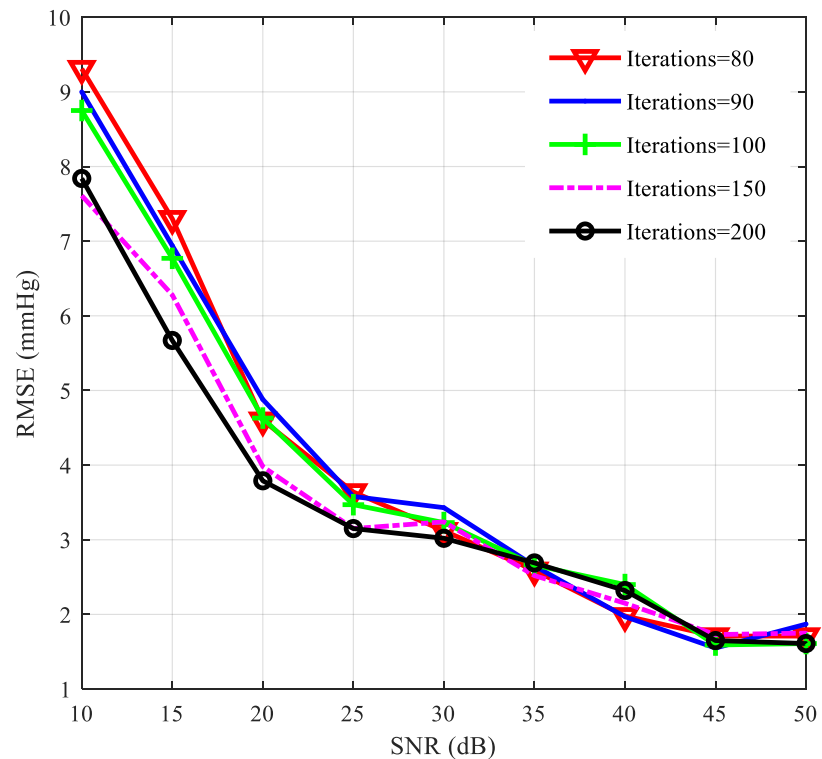


**Fig. 6.** Effect of iteration number on the relationship between RMSE and SNR, using the SKF algorithm.

All simulation results are summarized in Table 3. To simulate real in-vivo measurements where noise is inevitable, we applied the proposed SKF and CCA algorithms to estimate the  $P_a$  waveform by adding noise to  $P_p$  to produce a SNR of 25 dB. The RMSEs of the measured and estimated  $P_a$  were computed for the total waveform (TW), SP and beat-to-beat diastolic pressure (DP). For a SNR of 25 dB, it can be seen that the TW RMSE of the measured and estimated  $P_a$  waveforms using the CCA algorithm is  $6.43 \pm 2.66$  mmHg. However, the corresponding value obtained from the SKF algorithm is  $3.31 \pm 1.92$  mmHg.

**Table 3**

RMSEs obtained from measured and estimated  $P_a$  waveforms using the CCA and SKF algorithms at different added noise levels (Mean  $\pm$  SD).

| SNR (dB) | Method | TW (mmHg)        | SP (mmHg)        | DP (mmHg)           |
|----------|--------|------------------|------------------|---------------------|
| 10       | CCA    | $21.60 \pm 5.66$ | $30.9 \pm 12.95$ | $143.36 \pm 106.56$ |
|          | SKF    | $8.76 \pm 3.59$  | $5.28 \pm 2.26$  | $13.11 \pm 9.94$    |
| 15       | CCA    | $12.04 \pm 4.78$ | $13.45 \pm 7.61$ | $55.55 \pm 40.98$   |
|          | SKF    | $5.78 \pm 2.93$  | $2.46 \pm 1.45$  | $3.46 \pm 2.33$     |
| 20       | CCA    | $7.97 \pm 3.12$  | $5.38 \pm 2.00$  | $11.43 \pm 9.03$    |
|          | SKF    | $4.52 \pm 2.42$  | $1.44 \pm 0.78$  | $1.55 \pm 0.90$     |
| 25       | CCA    | $6.43 \pm 2.66$  | $2.27 \pm 0.97$  | $3.16 \pm 1.73$     |
|          | SKF    | $3.31 \pm 1.92$  | $0.93 \pm 0.42$  | $1.12 \pm 0.58$     |
| 30       | CCA    | $4.73 \pm 2.76$  | $1.16 \pm 0.56$  | $1.55 \pm 0.91$     |
|          | SKF    | $2.41 \pm 1.14$  | $0.77 \pm 0.22$  | $.99 \pm 0.43$      |
| 35       | CCA    | $3.89 \pm 2.52$  | $0.78 \pm 0.24$  | $1.03 \pm 0.45$     |
|          | SKF    | $2.25 \pm 1.57$  | $0.77 \pm 0.27$  | $0.89 \pm 0.30$     |
| 40       | CCA    | $1.95 \pm 1.14$  | $0.77 \pm 0.23$  | $0.87 \pm 0.32$     |
|          | SKF    | $1.46 \pm 0.79$  | $0.76 \pm 0.22$  | $0.81 \pm 0.21$     |
| 45       | CCA    | $1.26 \pm 0.80$  | $0.75 \pm 0.23$  | $0.80 \pm 0.20$     |
|          | SKF    | $1.29 \pm 0.65$  | $0.74 \pm 0.22$  | $0.79 \pm 0.18$     |
| 50       | CCA    | $1.06 \pm 0.49$  | $0.75 \pm 0.22$  | $0.76 \pm 0.19$     |
|          | SKF    | $1.19 \pm 0.54$  | $0.75 \pm 0.22$  | $0.76 \pm 0.22$     |

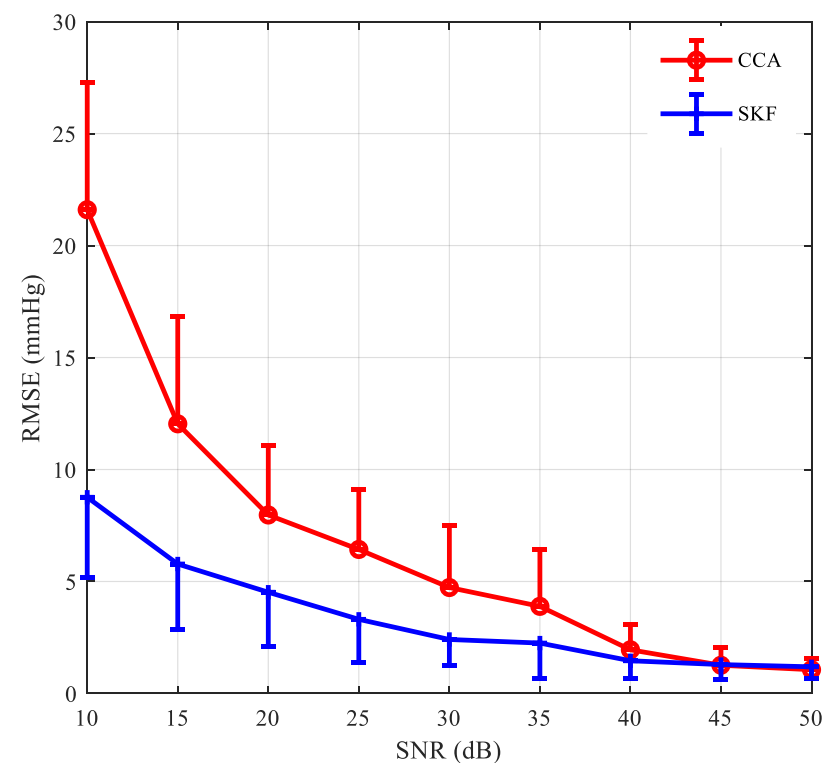


**Fig. 7.** Effect of added noise on the RMSE values obtained from measured and estimated  $P_a$  waveforms using the CCA and SKF algorithms (Mean  $\pm$  SD, the number of points in the total waveform,  $n$  is 600).

The two algorithms were compared by a paired t-test (IBM SPSS Statistics, version-23). The SKF algorithm has significantly lower RMSEs than the CCA up to an SNR of 40dB or maybe even 45dB. Fig. 7 shows that there was a significant difference between the CCA and SKF methods when the SNR values were less than 35 dB ( $p < 0.001$ ), although not for SNR values greater than 35 dB ( $p > 0.01$ ). In general, the results show that the SKF

method is more noise-tolerant than the CCA method. Fig. 8 compares the measured and estimated  $P_a$  waveforms using the CCA and SKF algorithms, operating on the same FIR simulation dataset. The correlation between the measured and estimated pressures is shown in Figs. 9 (A) and 10 (A) for the CCA and SKF algorithms, respectively. Also shown in each plot are the line of identity and the equation of the linear fit to the data. Figs. 9 (B) and 10 (B) are the corresponding Bland-Altman plots in which the mean bias is shown by the solid horizontal line and limits of agreement ( $\pm 1.96SD$  of the mean difference), by dashed lines.

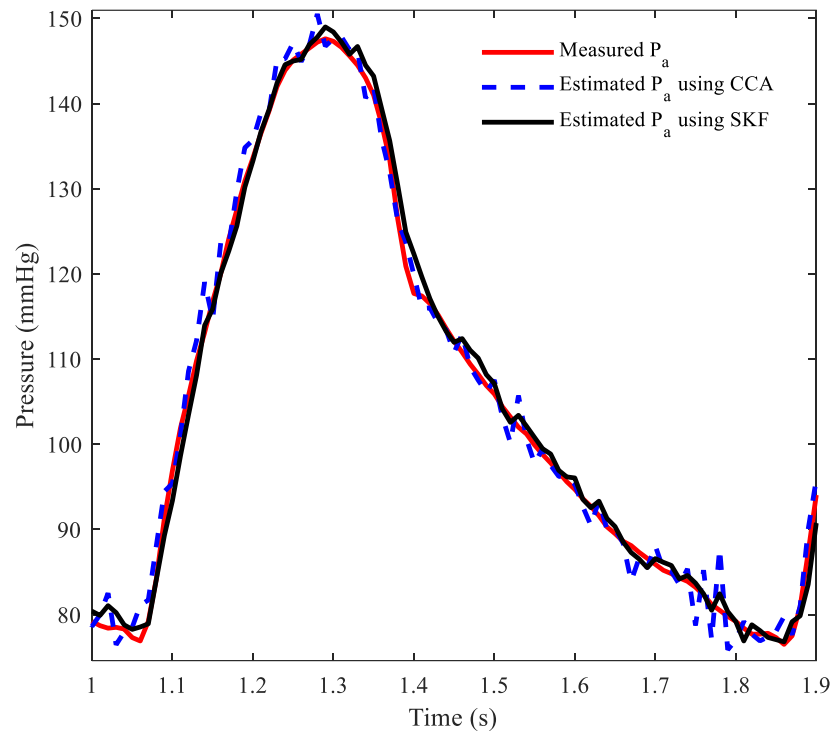


**Fig. 8.** Measured and estimated  $P_a$  waveforms using the CCA and SKF algorithms from the same subject for a SNR of 25 dB.

The linear regression equations obtained between the measured and estimated  $P_a$  waveforms using the CCA and SKF algorithms were  $y=1.00x-0.14$  ( $r=0.99$ ,  $p<0.001$ ) in Fig. 9 (A) and  $y=1.00x+0.28$  ( $r=0.99$ ,  $p<0.001$ ) in Fig. 10 (A). A comparison (mean  $\pm$  SD,  $-0.11 \pm 2.27$  mmHg) between the measured and estimated  $P_a$  waveforms using the CCA algorithm is shown in Fig. 9 (B); and a similar comparison using the SKF algorithm (mean  $\pm$  SD,  $-0.10 \pm 1.80$  mmHg) is shown in Fig. 10 (B).

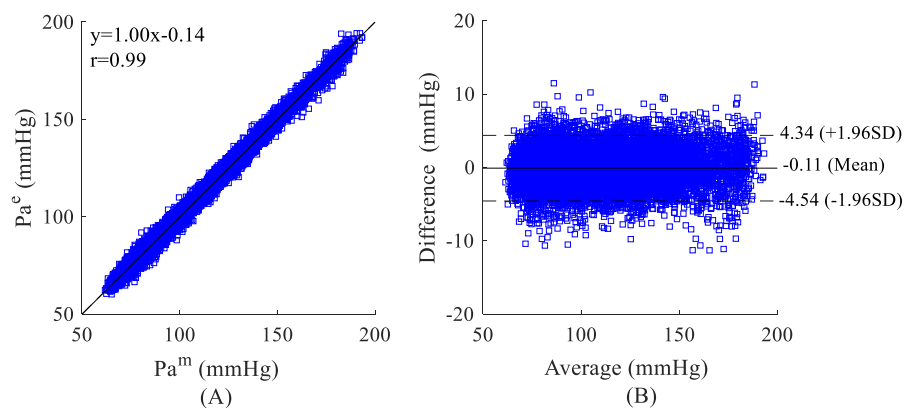


**Fig. 9.** (A) Correlation analysis and (B) Bland-Altman plots comparing measured and estimated  $P_a$  waveforms for a SNR of 25 dB using the CCA algorithm and FIR simulation data (25 subjects).  $P_a^m$  and  $P_a^e$  are the measured and estimated pressures, respectively.

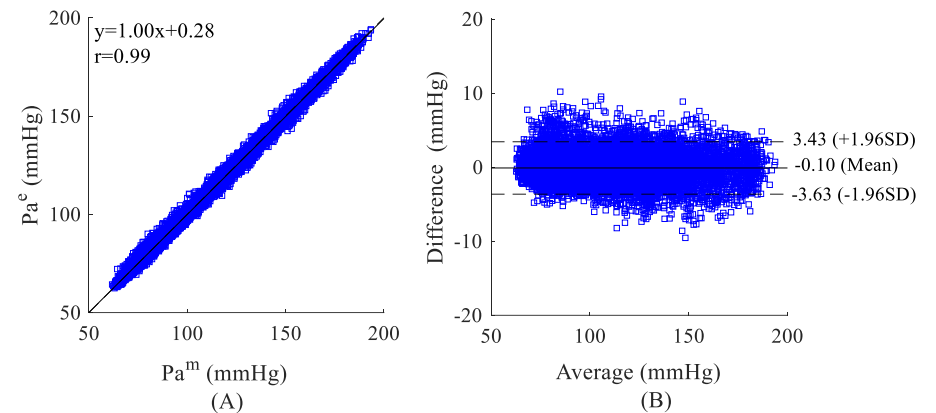


**Fig. 10.** (A) Correlation analysis and (B) Bland-Altman plots comparing measured and estimated  $P_a$  waveforms for a SNR of 25 dB using the SKF algorithm and FIR simulation data (25 subjects).  $P_a^m$  and  $P_a^e$  are the measured and estimated pressures, respectively.

### 3.2 Tube-load Modeling of arterial pressure waveforms in human subjects

As shown in Fig. 11, the SKF algorithm also has significantly lower RMSEs than the CCA. The proposed SKF algorithm clearly outperforms the CCA algorithm ( $p<0.001$ ). It is notable that, as shown in Fig. 11, the RMSE values of the measured and estimated  $P_a$  waveforms using the CCA algorithm are more than 5 mmHg for all values of SNR investigated. Thus, the mean difference between the estimated and measured  $P_a$  waveforms does not satisfy the Association for the Advancement of Medical Instrumentation standard of  $5 \pm 8$  mmHg [38], [39], whereas this requirement is met by the SKF approach, for SNRs of 25 dB and above. Again, a SNR of 25 dB, corresponding to a typical real-world value, has been used in Fig. 12 to provide a visual comparison of the performance of the two algorithms, where it is seen that the qualitative agreement between measured and estimated waveforms is good for the SKF algorithm but clearly inferior for the CCA approach.

Considering the tube-load simulation experiments, Table 4 shows that for SNRs greater than 25 dB there is little change in the RMSEs for SP and DP when calculated by either algorithm, although the SKF values remained consistently lower.

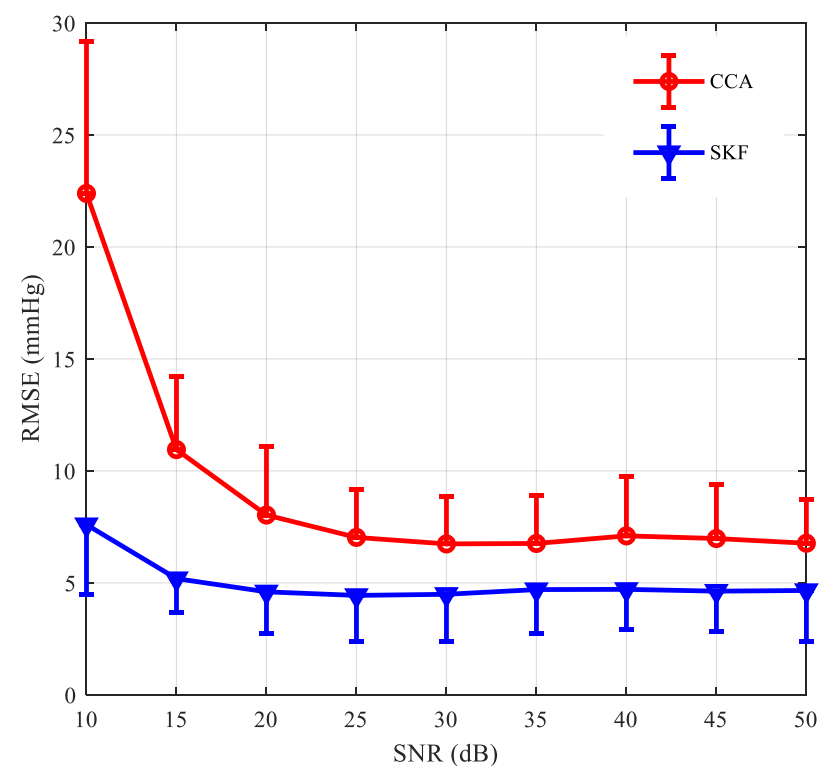


**Fig. 11.** Effect of added noise on the RMSE values obtained from measured and estimated  $P_a$  waveforms, using the CCA and SKF algorithms (Mean  $\pm$  SD, the number of points in the total waveform,  $n$  is 600).

When the SNR increases from 10 dB to 40 dB, the corresponding RMSE values for TW continue to decrease, as also listed in Table 4. Point-by-point comparisons of the pressure signals analyzed by the CCA and SKF algorithms are shown in the correlation plots of Figs.13 (A) and 14 (A), respectively. Also, in each plot the line of identity and the equation of the linear fit to the data are shown. Figs. 13 (B) and 14 (B) are the corresponding Bland-Altman plots in which the mean bias is shown by the solid horizontal line and limits of agreement ( $\pm 1.96SD$  of the mean difference), by dashed lines. The superior performance of the SKF approach is evident in the higher value of the Pearson correlation coefficient ( $r=0.99$ ,  $p<0.001$  vs.  $r=0.96$ ,  $p<0.001$ ) and the narrower limits of agreement ( $\pm 9.73$  mmHg vs.  $\pm 19$  mmHg).

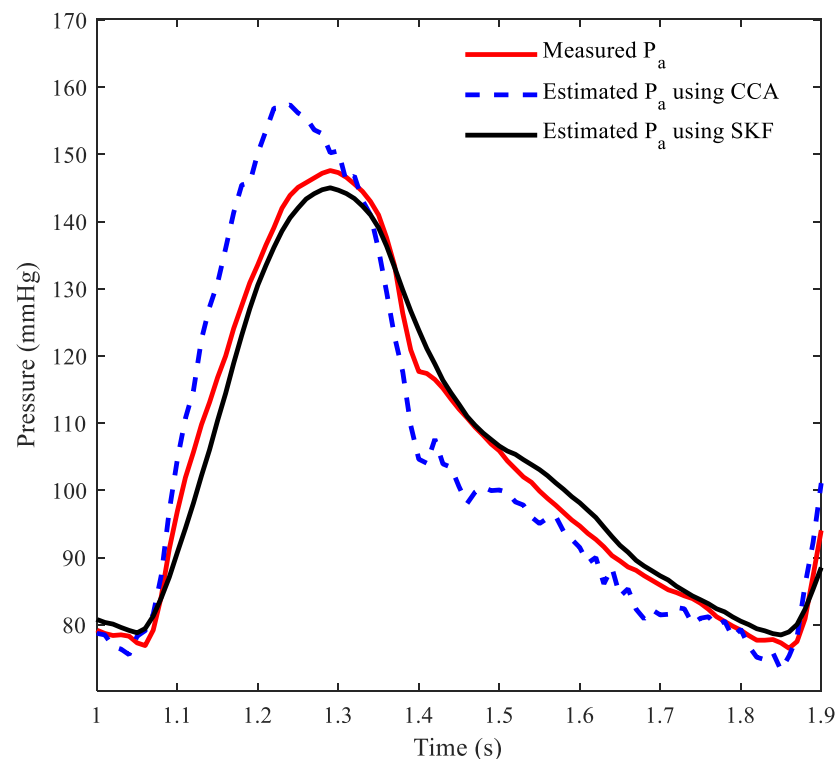


**Fig. 12.** Measured and estimated  $P_a$  waveforms using the CCA and SKF algorithms from the same subject for a SNR of 25dB.

**Table 4**

RMSE values are obtained from measured and estimated  $P_a$  waveforms using the CCA and SKF algorithms with the different SNRs of the observed channel output signals (Mean  $\pm$  SD).

| SNR (dB) | Method | TW (mmHg)        | SP (mmHg)         | DP (mmHg)          |
|----------|--------|------------------|-------------------|--------------------|
| 10       | CCA    | 22.39 $\pm$ 6.80 | 36.79 $\pm$ 11.91 | 122.09 $\pm$ 62.58 |
|          | SKF    | 7.59 $\pm$ 3.12  | 3.41 $\pm$ 2.35   | 4.10 $\pm$ 4.60    |
| 15       | CCA    | 10.95 $\pm$ 3.27 | 16.57 $\pm$ 6.02  | 31.45 $\pm$ 30.11  |
|          | SKF    | 5.19 $\pm$ 1.52  | 3.19 $\pm$ 1.79   | 1.70 $\pm$ 0.67    |
| 20       | CCA    | 8.03 $\pm$ 3.04  | 11.01 $\pm$ 5.03  | 9.02 $\pm$ 5.10    |
|          | SKF    | 4.60 $\pm$ 1.87  | 2.24 $\pm$ 1.47   | 1.24 $\pm$ 0.74    |
| 25       | CCA    | 7.03 $\pm$ 2.15  | 8.77 $\pm$ 4.85   | 2.87 $\pm$ 1.67    |
|          | SKF    | 4.43 $\pm$ 2.05  | 2.16 $\pm$ 1.57   | 0.96 $\pm$ 0.61    |
| 30       | CCA    | 6.74 $\pm$ 2.12  | 8.34 $\pm$ 5.00   | 1.72 $\pm$ 1.55    |
|          | SKF    | 4.49 $\pm$ 2.12  | 2.83 $\pm$ 2.45   | 0.82 $\pm$ 0.73    |
| 35       | CCA    | 6.76 $\pm$ 2.16  | 8.23 $\pm$ 4.93   | 1.33 $\pm$ 1.09    |
|          | SKF    | 4.71 $\pm$ 1.96  | 4.15 $\pm$ 3.66   | 0.64 $\pm$ 0.42    |
| 40       | CCA    | 7.10 $\pm$ 2.64  | 8.38 $\pm$ 5.09   | 1.34 $\pm$ 1.03    |
|          | SKF    | 4.68 $\pm$ 1.81  | 3.60 $\pm$ 3.50   | 0.72 $\pm$ 0.35    |
| 45       | CCA    | 6.98 $\pm$ 2.39  | 8.33 $\pm$ 5.08   | 1.22 $\pm$ 1.05    |
|          | SKF    | 4.63 $\pm$ 1.79  | 3.20 $\pm$ 3.27   | 0.81 $\pm$ 0.44    |
| 50       | CCA    | 6.77 $\pm$ 1.97  | 8.24 $\pm$ 4.97   | 1.14 $\pm$ 1.08    |
|          | SKF    | 4.66 $\pm$ 2.30  | 2.84 $\pm$ 2.60   | 0.98 $\pm$ 0.73    |

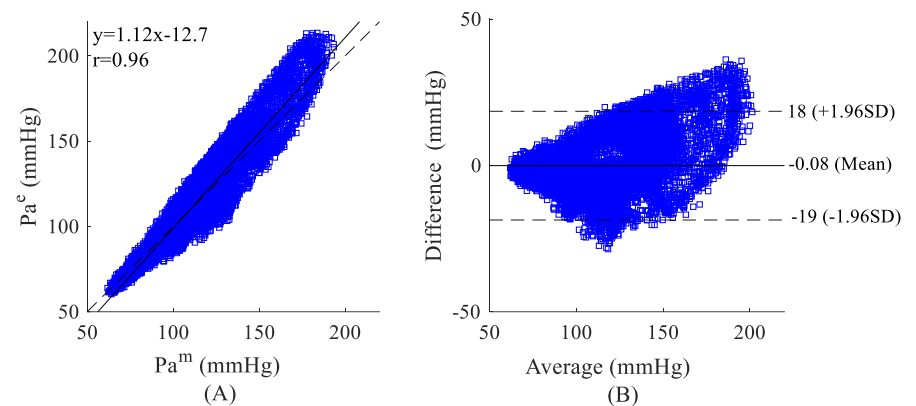


**Fig. 13.** (A) Correlation analysis and (B) Bland-Altman plots comparing measured and estimated  $P_a$  waveforms for a SNR of 25 dB using the CCA algorithm and FIR simulation data (25 subjects).  $P_a^m$  and  $P_a^e$  are the measured and estimated pressures, respectively.

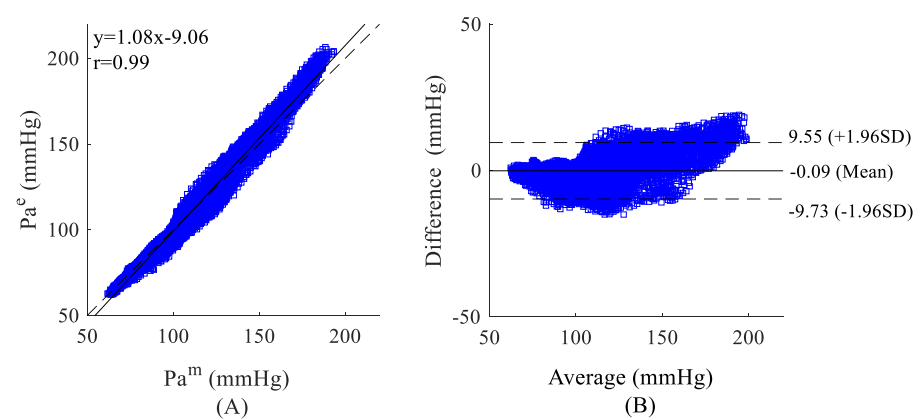


**Fig. 14.** (A) Correlation analysis and (B) Bland-Altman plots comparing measured and estimated  $P_a$  waveforms for a SNR of 25 dB using the SKF algorithm and FIR simulation data (25 subjects).  $P_a^m$  and  $P_a^e$  are the measured and estimated pressures, respectively.

### 3.3 Animal experiments

To verify the accuracy and effectiveness of the proposed SKF algorithm in vivo, we performed measurement on two Sprague-Dawley rats. The channel order was assumed to be 20 and the number of points in the total waveform of every sample was 1800. The estimated and true pressure waveforms agreed well. The average RMSE of the total waveform between the measured and estimated  $P_a$  waveforms using the SKF algorithm was 1.20 mmHg and that using the CCA algorithm, 1.70 mmHg.

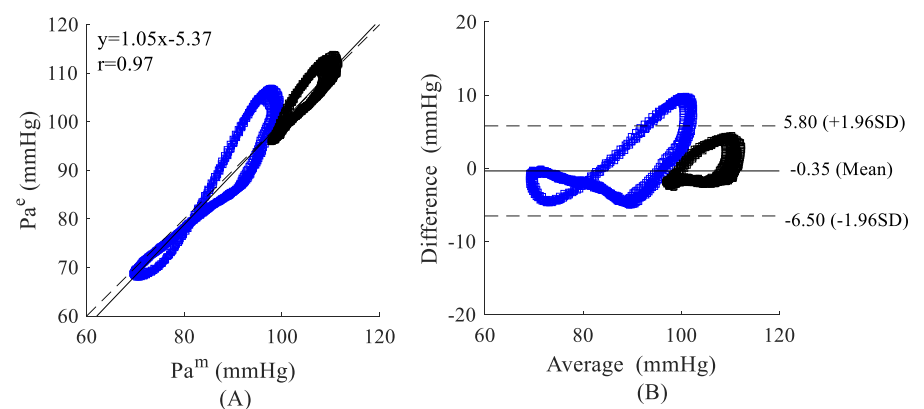


**Fig. 15.** (A) Correlation analysis and (B) Bland-Altman plots comparing measured and estimated  $P_a$  waveforms using the CCA algorithm (2 Sprague-Dawley rats). Animal<sub>1</sub>, blue points; animal<sub>2</sub>, black points.  $P_a^m$  and  $P_a^e$  are the measured and estimated pressures, respectively.

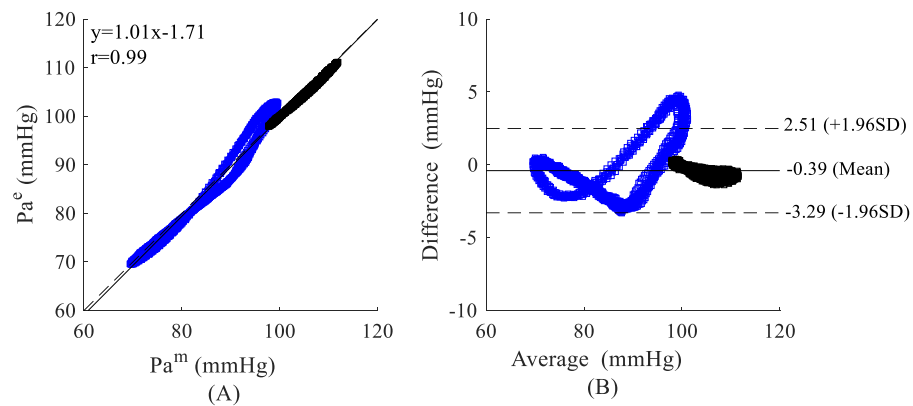


**Fig. 16.** (A) Correlation analysis and (B) Bland-Altman plots comparing measured and estimated  $P_a$  waveforms using the SKF algorithm (2 Sprague-Dawley rats).

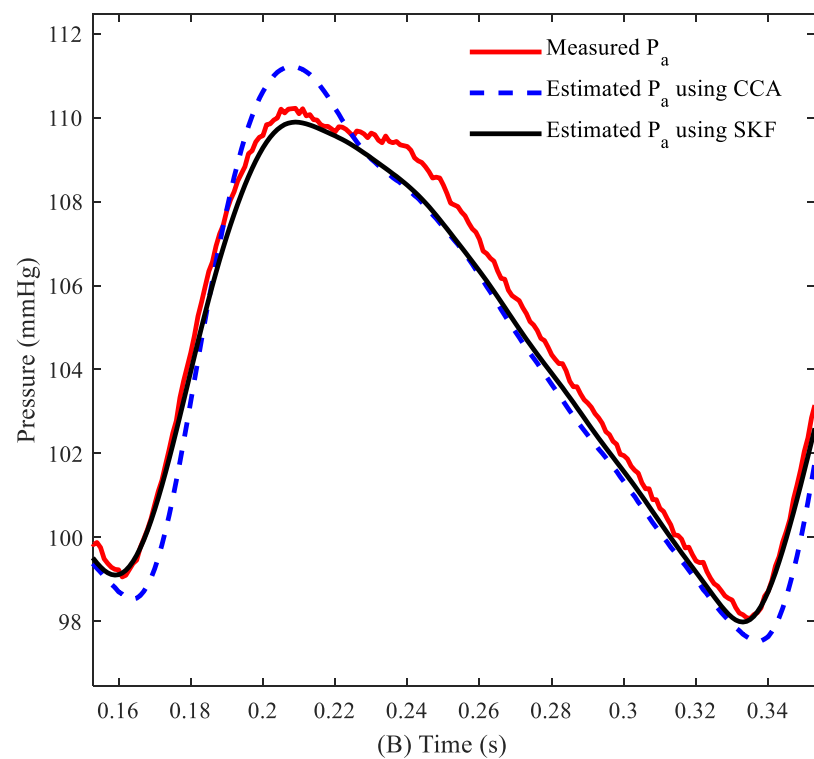
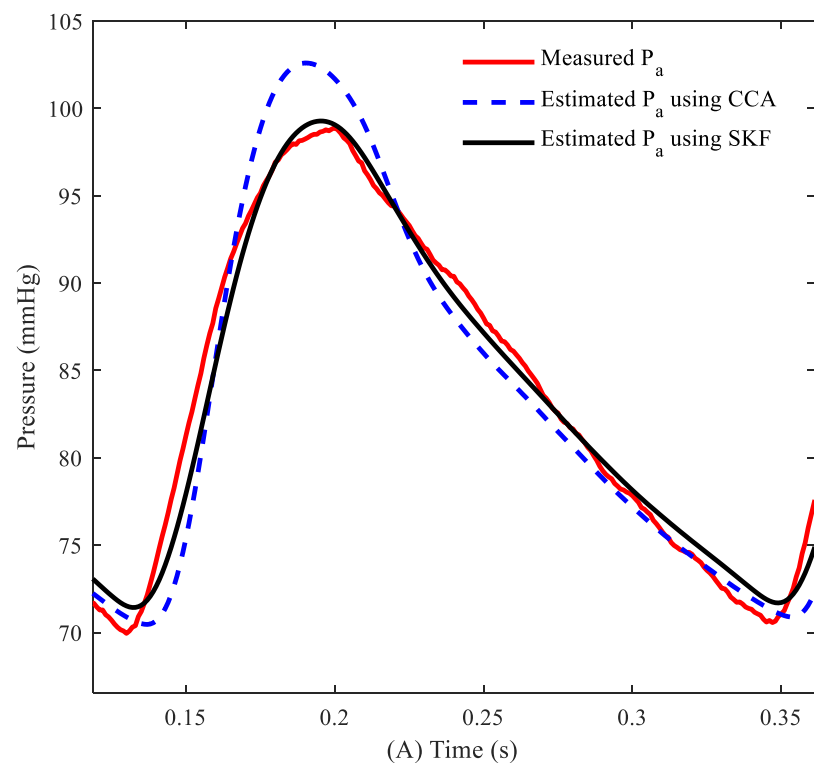


**Fig. 17.** Measured and estimated  $P_a$  waveforms using the CCA and SKF algorithms from 2 Sprague-Dawley rats (A and B).

The point-by-point correlation and corresponding Bland Altman plots (Figs. 15 and 16) again show that the SKF algorithm yields a higher correlation coefficient ( $r=0.99$ ,  $p<0.001$  vs.  $r=0.97$ ,  $p<0.001$ ) as well as narrower limits of agreement ( $\pm 3.29$  mmHg vs.  $\pm 6.50$  mmHg). Fig. 17 is a visual comparison of the two algorithms and shows that the estimated  $P_a$  waveform using the SKF algorithm is closer to the measured  $P_a$  waveform than that obtained from the CCA algorithm, most notably near end systolic and end diastolic pressure.

#### 4. Discussion

In this study, we have applied a simplified Kalman filter algorithm to estimate central  $P_a$  in simulations and in-vivo experiments and compared the results to those obtained from the previously described CCA approach. In the simulations, we have shown that, although the results are similar at high SNRs, when the signal becomes relatively weaker the SKF algorithm outperforms the CCA algorithm. Furthermore, the proposed SKF algorithm for central  $P_a$  estimation does not require any explicit calibration as the method is by nature self-calibrating and can thus account for any inter-subject or intra-subject variability in vascular dynamics.

In the simulation experiments, the convergence performance of the SKF algorithm has shown that the NPM values decrease markedly as the SNR increases. The convergence is fast and the channel impulse responses are accurately estimated when the SNR is high, as shown in Fig. 5. The results also demonstrate that the RMSEs decrease as the number of iterations increases, as shown in Fig. 6, where the number of iterations ranges from 80 to 200. It was found that if the number of iterations is less than the number of sampling points in one complete cardiac cycle, the  $P_a$  waveform cannot be reliably reproduced. Therefore, the number of iterations was maintained at a value not less than 80. For lower values of SNR, RMSEs fall with increasing number of iterations; although for SNRs greater than 30 dB, increasing the number of iterations had little further effect. Fig. 6 also shows that there is a small additional gain in performance when the number of iterations is increased from 150 to 200, the effect being more marked for low SNRs. These results indicate that the proposed SKF algorithm has a good overall performance when the number of iterations is 150 or more. Accordingly, to optimize the speed and accuracy in estimating the  $P_a$  waveform, the number of iterations of the SKF algorithm was set to 200. On the whole, TW RMSEs of the measured and estimated  $P_a$  waveforms using the SKF algorithm are lower than those seen when using the CCA algorithm. Moreover, the SKF algorithm gives lower RMSE values for SP and DP, as shown in Tables 3 and 4. For the animal experiments, although the proposed SKF algorithm outperforms the CCA method, only two animals were measured, so this result should be regarded only as preliminary.

There are other limitations to the study. Although the aortic and brachial blood pressure measurements in our previous study were collected simultaneously, we did not record any additional peripheral pressures at the same time. The nonlinearity of the cardiovascular system is neglected, which may lead to some estimation errors, such as notch point error and reflection point error, both of which will affect clinically important hemodynamic variables such as augmentation index, reflection magnitude and reflection index.

#### 5. Conclusion

The results of the simulation experiments demonstrate that the performance of MBSI algorithms based on the proposed SKF approach is superior to that of the CCA method over a wide range of SNRs in the observed signal. The results of the animal experiments also confirm that the proposed SKF algorithm is superior to the CCA algorithm. It is worth



noting that the SKF algorithm is especially effective for estimating systolic and diastolic pressures, which from the clinician's point of view, as a measure of cardiac load, is of particular value. In a future study, we will measure more animals for the in-vivo validation of the SKF approach. We also plan to develop a nonlinear blind identification algorithm as an alternative approach to the estimation of central pressure from peripheral measurements.

### Declaration of competing interest

The authors declare that they have no conflict of interests.

### Acknowledgments

This work was supported by the National Key Research and Development Program of China (No. 2017YFC1307600), the National Natural Science Foundation of China (No. 61773110), and the Fundamental Research Funds for the Central Universities (No. N2119008). This research was also supported by the Shenyang Science and Technology Plan Fund (No. 20-201-4-10), the Member Program of Neusoft Research of Intelligent Healthcare Technology, Co. Ltd. (No. MCMP062002).

### Abbreviations

|       |                                          |
|-------|------------------------------------------|
| CCA   | Canonical correlation analysis           |
| CR    | Cross-relation                           |
| $C_T$ | Compliance of the distal arteries        |
| DP    | Diastolic pressure                       |
| FIR   | Finite impulse response                  |
| MBSI  | Multichannel blind system identification |
| NPM   | Normalized projection misalignment       |
| $P_a$ | Aortic pressure                          |
| $P_b$ | Peripheral artery pressure               |
| $P_f$ | Femoral pressure                         |
| $P_p$ | Peripheral artery pressure               |
| $P_r$ | Radial pressure                          |
| $R_T$ | Peripheral resistance                    |
| RMSE  | Root mean square error                   |
| SIMO  | Single input multiple output             |
| SKF   | Simplified Kalman filter                 |
| SP    | Systolic pressure                        |
| SS    | Subspace                                 |
| TW    | Total waveform                           |
| $Z_c$ | Characteristic impedance                 |
| $Z_L$ | Terminal impedance                       |

### References

- [1] W. Bryan, *et al.*, 2018 ESC/ESH Guidelines for the management of arterial hypertension: the task force for the management of arterial hypertension of the European Society of Cardiology (ESC) and the European Society of Hypertension (ESH). *European heart journal*, vol. 39, no. 33, pp. 3021-3104, 2018.
- [2] P. Salvi. Pulse waves. *Springer International Publishing*, 2nd ed. 2017.
- [3] W. W. Nichols *et al.*, "McDonald's blood flow in arteries: theoretical, experimental and clinical principles," in *Hodder Arnold*, 6th ed. London, 2011.
- [4] A. P. Avolio *et al.*, "Arterial blood pressure measurement and pulse wave analysis-their role in enhancing cardiovascular assessment," *Physiological Measurement*, vol. 31, no. 1, pp. 1-47, Jan. 2009.
- [5] W. W. Nichols *et al.*, "Effects of arterial stiffness, pulse wave velocity, and wave reflections on the central aortic pressure waveform," *Journal of Clinical Hypertension*, vol. 10, no. 4, pp. 295-303, Apr. 2008.
- [6] M. J. Roman *et al.*, "Relations of central and brachial blood pressure to left ventricular hypertrophy and geometry: the strong heart study," *Journal of Hypertension*, vol. 28, no. 2, pp. 384-388, Feb. 2010.
- [7] C. M. Mceniery *et al.*, "Central blood pressure: current evidence and clinical importance," *European Heart Journal*, vol. 35, no. 26, pp. 1719-1725, Jul. 2014.
- [8] T. Y. Cai *et al.*, "Central blood pressure in children and adolescents: non-invasive development and testing of novel transfer functions," *Journal of Human Hypertension*, vol. 31, no. 12, pp. 831-837, Aug. 2017.
- [9] C. H. Chen *et al.*, "Validation of carotid artery tonometry as a means of estimating augmentation index of ascending aortic pressure," *Hypertension*, vol. 27, no. 2, pp. 168-175, Feb. 1996.
- [10] R. Kelly *et al.*, "Noninvasive carotid pressure wave registration as an indicator of ascending aortic pressure," *Journal of Vascular Medicine Biology*, vol. 1, pp. 241-247, Jan. 1989.
- [11] F. Michael *et al.*, "Noninvasive studies of central aortic pressure," *Current Hypertension Reports*, vol. 14, no. 1, pp. 8-20, Feb. 2012.
- [12] Y. T. Shih *et al.*, "Quantification of the calibration error in the transfer function-derived central aortic blood pressures," *American Journal of Hypertension*, vol. 24, no. 12, pp. 1312-1317, Aug. 2011.
- [13] G. Zhang *et al.*, "Tube-load model parameter estimation for monitoring arterial hemodynamics," *Frontiers in Physiology*, vol. 2, no. 72, pp. 1-18, Nov. 2011.
- [14] M. Rashedi *et al.*, "Comparative study on tube-load modeling of arterial hemodynamics in humans," *Journal of Biomechanical Engineering*, vol. 135, no. 3, pp. 1-9, Mar. 2013.
- [15] O. Narayan *et al.*, "Estimation of central aortic blood pressure," *Journal of Hypertension*, vol. 32, no. 9, pp. 1727-1740, Jun. 2014.
- [16] Shih YT, *et al.*, "Comparison of two generalized transfer functions for measuring central systolic blood pressure by an oscillometric blood pressure monitor," *Journal of Human Hypertension*, vol. 27, no. 3, pp.204-210, 2013.
- [17] B. E. Westerhof *et al.*, "Individualization of transfer function in estimation of central aortic pressure from the peripheral pulse is not required in patients at rest," *Journal Applied Physiology*, vol. 105, no. 6, pp. 1858-1863, Oct. 2008.
- [18] Y. Zhang and H. Asada, "Blind system identification of coprime multichannel systems and its application to noninvasive cardiovascular monitoring," *ASME Journal of Dynamic Systems: Measurement and Control*, vol. 126, no. 4, pp. 834-847, Dec. 2004.
- [19] Q. Mayyala *et al.*, "Structure-based subspace method for multi-channel blind system identification," *IEEE Signal Processing Letters*, vol. 24, no. 8, pp. 1183-1187, Feb. 2017.
- [20] A. Patel *et al.*, "Aortic pressure estimation using blind identification approach on single input multiple output nonlinear wiener systems," *IEEE Transactions on Biomedical Engineering*, vol. 65, no. 6, pp. 1193-1200, Jun. 2018.
- [21] T. Mei, "Blind multichannel identification based on Kalman filter and eigenvalue decomposition," *International Journal of Speech Technology*, vol. 22, no. 1, pp. 1-11, Mar. 2019.
- [22] L. Xu *et al.*, "Baseline wander correction in pulse waveforms using wavelet-based cascaded adaptive filter," *Computers in Biology and Medicine*, vol. 37, no. 5, pp. 716-731, May. 2007.
- [23] W. Huh, *et al.*, "Development of pulse rate detection system for oriental medicine," in *Proceedings of 19<sup>th</sup> International Conference-IEEE/EMBS*, October 1997, pp. 2406-2408.
- [24] Y. Yao *et al.*, "Validation of an adaptive transfer function method to estimate the aortic pressure waveform," *IEEE Journal of Biomedical & Health Informatics*, vol. 21, no. 6 pp. 1599-1606, Nov. 2017.
- [25] R. Burattini and K. B. Campbell, "Modified asymmetric T-tube model to infer arterial wave reflection at the aortic root," *IEEE Transactions on Biomedical Engineering*, vol. 36, no. 8, pp. 805-814, Aug. 1989.
- [26] M. K. Abed *et al.*, "Blind system identification," *Proceedings of the IEEE*, vol. 85, no. 12, pp. 1310-1332, Sep. 1997.
- [27] M. I. Gurelli and C. L. Nikias, "A new eigenvector-based algorithm for multichannel blind deconvolution of input coloured signal," in *IEEE International Conference on Acoustics*. 1993. no. April, pp. 448-451.
- [28] M. Lustig *et al.*, "Compressed sensing MRI," *IEEE Signal Process. Mag.*, vol. 25, no. 2, pp. 72-82, 2008.
- [29] F. J. Herrmann and G. Hennenfent, "Non-parametric seismic data recovery with curvelet frames," *Geophysical Journal International*, vol. 173, no. 1, pp. 233-248, 2008.
- [30] Y. Sato, "A method of self-recovering equalization for multilevel amplitude-modulation systems," *IEEE Transactions on Communications*, vol. 23, no. 6, pp. 679-682, 2008.
- [31] D. Godard, "Self-recovering equalization and carrier tracking in two-dimensional data communication systems," *IEEE Transactions on Communications*, vol. 28, no. 11, pp. 1867-1875, 1980.
- [32] J. J. Shynk *et al.*, "Comparative performance study of several blind equalization algorithms," *Proceedings of SPIE*, vol. 1565, pp. 102-117, 1991.
- [33] S. G. Shroff *et al.*, "Physiological relevance of T-tube model parameters with

- emphasis on arterial compliances,” *American Journal of Physiology-Heart and Circulatory Physiology*, vol. 269, no. 2, pp. 365-374, Aug. 1995.
- [34] K. B. Campbell *et al.*, “Time-domain formulation of asymmetric T-tube model of arterial system,” *American Journal of Physiology-Heart and Circulatory Physiology*, 258(6 Pt 2), pp. 1761-1774, 1990.
- [35] P. Segers *et al.*, “Individualizing the aorto-radial pressure transfer function: feasibility of a model-based approach,” *American Journal of Physiology-Heart and Circulatory Physiology*, vol. 279, no. 2, pp. 542-549, 2000.
- [36] D. R. Morgan *et al.*, “On the evaluation of estimated impulse responses,” *IEEE Signal Process Lett*, vol. 5, no. 7, pp. 174-176, 1998.
- [37] M. K. Hasan *et al.*, “Improving robustness of blind adaptive multichannel identification algorithms using constraints,” in *European Signal Processing Conference. IEEE*, 2005, no. September, pp. 4-8.
- [38] Y. T. Shih *et al.*, “Application of the N-point moving average method for brachial pressure waveform-derived estimation of central aortic systolic pressure,” *Hypertension*, vol. 63, no. 4, pp. 865-870, Apr. 2014.
- [39] E. O’Brien *et al.*, “Working group on blood pressure monitoring of the European society of hypertension international protocol for validation of blood pressure measuring devices in adults,” *Blood Pressure Monitoring*, vol. 7, no. 1, pp. 3-17, 2002.
- [40] W. Liu *et al.*, “Aortic pressure waveforms reconstruction using simplified Kalman filter,” in *Computing in Cardiology*, 2019, no. September, pp. 1-4.